Using ambient seismic noise to monitor ocean bottom pressure

Bingxu Luo[1], Shuo Zhang[1], Nozomu Takeuchi[2], David Lumley[1,3], and Hejun Zhu[1,3]

[1]Department of Sustainable Earth System Sciences, The University of Texas at Dallas
[2]Earthquake Research Institute, The University of Tokyo
[3]Department of Physics, The University of Texas at Dallas

March 21, 2024

Abstract

Ambient seismic noise (ASN) recorded by ocean bottom seismometers allows us to perform coda wave interferometry without using active sources. We analyzed two-year ASN recordings from five ocean bottom stations in the northwestern Pacific Ocean basin (depth > 5,500 m), and measured the relative velocity variation ($\delta v/v$) near the seafloor. The most important finding is an extremely low variation in $\delta v/v$ (around -0.05\%), which likely responds to a significant pressure drop at sea level and subsequently affects an anomaly at the ocean bottom (over -400 Pa) in December 2013. Furthermore, several major phases of the velocity change show delayed-correlation with the sea level pressure variations. A poroelastic simulation with adjusted ocean bottom variables supports the pressure factor mainly drives the variation in $\delta v/v$. Our study suggests the potential use of seismic signals to monitor oceanic and atmospheric processes by tracking variations in the oceanic pressure field.

Using ambient seismic noise to monitor ocean bottom pressure

Bingxu Luo[1], Shuo Zhang[1], Nozomu Takeuchi[3], David Lumley[1,2] and Hejun Zhu[1,2,*]

[1]Department of Sustainable Earth System Sciences, The University of Texas at Dallas

[2]Department of Physics, The University of Texas at Dallas

[3]Earthquake Research Institute, The University of Tokyo

Key Points:

- Our measured relative velocity variation ($\delta v/v$) shows a significant decrease that correlates with the ocean bottom pressure.
- An adapted poroelastic model supports that the measured $\delta v/v$ may be induced by the ocean bottom pressure field.
- This ambient seismic noise measurement reflects regional atmospheric activities.

Corresponding author: Hejun Zhu, hejun.zhu@utdallas.edu

Abstract

Ambient seismic noise (ASN) recorded by ocean bottom seismometers allows us to perform coda wave interferometry without using active sources. We analyzed two-year ASN recordings from five ocean bottom stations in the northwestern Pacific Ocean basin (depth >5,500 m), and measured the relative velocity variation ($\delta v/v$) near the seafloor. The most important finding is an extremely low variation in $\delta v/v$ (around -0.05%), which likely responds to a significant pressure drop at sea level and subsequently affects an anomaly at the ocean bottom (over -400 Pa) in December 2013. Furthermore, several major phases of the velocity change show delayed-correlation with the sea level pressure variations. A poroelastic simulation with adjusted ocean bottom variables supports the pressure factor mainly drives the variation in $\delta v/v$. Our study suggests the potential use of seismic signals to monitor oceanic and atmospheric processes by tracking variations in the oceanic pressure field.

Plain Language Summary

Passive seismic techniques are increasingly being used to monitor complex environmental changes due to their high sensitivity, continuous sampling and relatively low costs. In this study, we utilize ambient seismic noise recorded by ocean bottom seismometers to continuously monitor velocity changes near the seafloor. We observe a clear consistency between the measured seismic velocity changes and variations in ocean bottom pressure, which can be attributed to atmospheric changes. The most important contribution of our study is to suggest the potential of using seismic measurements to monitor physical processes occurring in the ocean bottom and atmosphere. Seismic remote sensing of variations in the oceanic pressure field can be further improved by utilizing higher quality datasets and may help bridge the spatiotemporal resolution gaps in current space-borne monitoring approaches.

Introduction

Ambient seismic noise (ASN) includes microseisms generated by ground surface motions that are not caused by earthquakes or explosions (Gutenberg, 1958). High frequency noise (>1 Hz) is mainly caused by human activities, such as industry and traffic (Campillo & Roux, 2015). On the other hand, low-frequency noise (<1 Hz) is primarily due to natural sources, such as oceanic swells and their interaction with the solid Earth. These sources are commonly found in both coastal regions and deep oceans (Nishida et al., 2008; Campillo & Roux, 2015). By leveraging the global distribution of ASN sources, we can use interferometry between ASN recorded by two stations to approximate the impulsive response of the medium, known as the Green's function. This technique has been developed as an efficient passive method for seismic tomography (Shapiro et al., 2005; Sabra et al., 2005; Yao et al., 2006; Yang et al., 2007; Lin et al., 2007), which allows us to image the crust and uppermost mantle structure by measuring group and phase velocities of dispersive surface waves in tectonically inactive areas. Another recent application of ASN is to measure the relative velocity variation ($\delta v/v$) in the near-surface. Unlike tomography, this technique directly measures the velocity change based on the traveltime shift between two Green's functions within the coda wave (scattered multiple times in the heterogeneous medium) windows for two different dates. The $\delta v/v$ technique has been widely used to monitor environmental changes and tectonic activities, as it is based on the high pressure sensitivity of seismic wave speeds in an elastic medium (Dvorkin & Nur, 1996; Dvorkin et al., 1999; Saul et al., 2013). It can provide insights into temperature changes (Meier et al., 2010), ice sheets melting (Mordret et al., 2016; Toyokuni et al., 2018; Luo et al., 2023), terrestrial water storage (Lecocq et al., 2017; Mao et al., 2022; Zhang et al., 2023), atmospheric pressure (Gradon et al., 2021), fault zone and volcanic activities (Sens-Schönfelder & Wegler, 2006a; Wegler & Sens-Schönfelder, 2007; Brenguier et al., 2008). This in-situ and high-sensitivity monitoring approach provides us with a novel way to investigate the complex processes of the near-surface at different temporal and spatial scales.

Recently, Wu et al. (2020) used traveltime differences of tertiary arrivals (after P and S waves) generated by repeating earthquakes (doublets) to monitor basin-scale ocean temperature variations. This study suggests that seismic velocity changes are sensitive enough to monitor temperature changes within deep oceans (>2,000 m). In our study, we aim to explore the bottom of ocean basins, an area that has not been well investigated and involves complicated water-seafloor interaction. Thanks to the Normal Ocean Mantle (NOMan) Project, operated by the Earthquake Research Institute at The University of Tokyo, we have the opportunity to utilize continuous ocean bottom seismic (OBS) recordings to monitor the deep seafloor. We collect two-year ASN recordings from five OBSs within the northwestern Pacific Ocean basin (>5,500 m depth). We apply the passive $\delta v/v$ technique to the coda wave windows of the measured cross-correlation function between each station pair. We attempt to interpret the measured $\delta v/v$ time series with various deep ocean physical variables, such as temperature, salinity and pressure. We propose that the low $\delta v/v$ variation may be due to a low ocean bottom pressure anomaly observed in December, 2013. Moreover, several consistent phases between sea level pressure and $\delta v/v$ variations suggest that the atmospheric pressure field likely dominates the ocean bottom pressure variations, which directly controls the near-seafloor $\delta v/v$ changes. We then use a poroelastic mechanism to explain the $\delta v/v$ variations. The consistent magnitudes and phases between our measurements and the end-member model further support our interpretation. Our study demonstrates that the $\delta v/v$ technique can be used to monitor deep ocean pressure changes, which are not easily observed by using conventional in-situ or remote sensing approaches.

Data and methods

Ocean bottom seismographic recordings

We obtain continuous ocean bottom seismic recordings from the NOMan Project (Matsuno et al., 2017). This array consists of eighteen ocean bottom seismometers (OBS).

We select five of them (NM01 to NM05) with over two-year continuous records, they are deployed at depths exceeding 5,500 m below the sea surface, in the northwestern Pacific Ocean (Figure 1A). These five stations are spaced apart at distance ranging from 109 to 249 km. Throughout the study period, three of these five stations were shifted during the system replacement due to the battery lifetime. These relocations are not considered here due to their relatively small shifts of 1.51, 0.17 and 0.06 km. We collect continuous recordings from all five stations for a period of two years, from August 2012 to August 2014. All stations are equipped with broadband instruments and have a sampling rate of 100 Hz.

Near-seafloor $\delta v/v$ measurements

We use the MSNoise package (Lecocq et al., 2014) to achieve ASN interferometry and $\delta v/v$ measurements. First, we apply the preprocesses of demeaning, detrending, and a bandpass filter of 0.05 to 2 Hz to all seismograms. Only the vertical components of five stations are used for cross-correlate with each other. We set the analysis duration as 86,400 s (one day) and cut each seismogram into 1,800 s (30-minute) slices (with a 50 % overlap). We use three times of the root mean square (RMS) amplitude of the slice as extreme limits to suppress outliers (e.g., earthquake arrivals), and spectral whitening is applied to each correlation slice. Then, we retrieve all daily noise correlation functions (NCFs), and stack them together to obtain the reference signal. Next, we use a moving-window cross-spectrum (MWCS) technique (Ratdomopurbo & Poupinet, 1995; Clarke et al., 2011) to measure the temporal evolution of $\delta v/v$. This MWCS technique takes advantage of the similarity of Fourier phase spectra between the daily and referenced NCFs, and measures time shifts in unwrapped phases by solving a linear regression problem. Figure 2 shows an example of the measured time shifts (δt) between the daily and reference NCFs for the station pair NM01-NM03. In each daily measurement, the fitted slope, using selected δt, is considered as the daily time shift ($\delta t/t$) (Figure S1d). If we assume the velocity perturbation is homogeneous between the two stations, we have the following relation:

$$\delta v/v = -\delta t/t \quad . \tag{1}$$

This MWCS technique has been proven to perform better than time-domain techniques, such as waveform stretching or dynamic warping (Sens-Schönfelder & Wegler, 2006b; Meier et al., 2010), since it mitigates possible biases due to amplitude spectra changes from noise sources (Clarke et al., 2011; Zhan et al., 2013). More details about the MWCS technique and the parameters we use can be found in supplementary Text S1 and Table S1, and Figure S1 shows an example of the MWCS workflow.

Robustness of the $\delta v/v$ measurements

First, we would like to evaluate the effects of various technical factors during data processing and $\delta v/v$ measurements. We begin by testing different frequency ranges used in $\delta v/v$ measurements (Figure S2). From low to high frequency ranges (0.1-0.5, 0.1-0.8, 0.3-1 and 0.5-1.2 Hz), the long-term trends of the measured $\delta v/v$ are generally consistent with each other. However, the measurements from the higher and lower frequency bands include more high frequency noise or have lower sensitivity, which can potentially obscure the measured $\delta v/v$. Next, we estimate the depth sensitivity kernels to better constrain our tests. Here, we assume that the measured $\delta v/v$ are primarily scattered (early coda arrivals) from the Scholte waves, which are reconstructed as the coherent energy in the NCFs (Figures S1a and b). The Scholte waves are typical surface waves that propagate at the interface between a liquid and an elastic solid medium (Scholte, 1947). The sensitivity kernels demonstrate that 0.8 Hz can provide sufficiently high sensitivity to the near-seafloor (Figure S3). Therefore, we choose the measurement from the 0.1-0.8 Hz passband as a balanced compromise between measurement sensitivity and quality.

It has been widely recognized that window selection is quite important when we measure traveltime differences using MWCS analysis (Zhan et al., 2013; Lecocq et al., 2014). Here, we select 80 s windows on both sides of the NCFs by considering different phase velocities (0.8, 1.0, 1.2, 1.5 km/s), which include signals from direct to coda arrivals within the NCFs. In Figure S4, we observe the high similarity of measured $\delta v/v$ by using two early coda wave windows (1.0 and 1.2 km/s). In contrast, the measured $\delta v/v$ from direct and later coda wave windows (1.5 and 0.8 km/s) show strange velocity changes compared to the former. The window selection directly determines data with smaller misfits are used for $\delta t/t$ fitting, and do not bias the regression further (Figure S1d). Therefore, we selected the window using a velocity of 1.0 km/s and a length of 80 s to achieve reliable $\delta v/v$ measurements.

Here, we further test the spatial distribution of noise source energy by using a Matched Field Processing (MFP) algorithm (Bucker, 1976; Igel et al., 2023). We selected a typical velocity of 1.4 km/s, which represents the coherent energy arrivals in our observations (Figure S4a). We used this velocity to calculate the traveltime differences between station pairs and a potential source grid. Next, we back-projected the stacked enveloped energy from NCFs into all grids of the source space. We separately calculated the MFP power maps for four different days of different seasons (Figure S5). These four representative stacked MFP power maps suggest that the dominant localized source energy comes from the northwest directions, despite some imaging artifacts due to the limited number of stations (Figure S5b). The observed uneven noise source distribution can explain the asymmetric causal and acausal NCFs for most station pairs (Figures S4a and S5a). The MFP test suggests that the localization of noise source energy is stable, which has been proven to satisfy robust $\delta v/v$ monitoring (Hadziioannou et al., 2009). Thus, we conclude that the measured $\delta v/v$ is unlikely to be biased by instability in the noise source distribution.

Results

The most important feature of the measured $\delta v/v$ is an anomalous low variation (-0.05 %) in February 2014 (Figure 1B), which represents the regional-median value across all station pairs. We also note that the $\delta v/v$ anomaly varies for different station pairs (Figure 1A). For instance, the station pair NM01-NM03 has the largest $\delta v/v$ anomaly with a value of -0.10 %, which covers a sub-area towards the southeast. Previous studies have shown that one important factor that drives variations in near-surface velocity is the change of surface stress/strain fields. Therefore, we collect the regional ocean bottom pressure (OBP) variation from Gravity Recovery and Climate Experiment (GRACE) satellites monitoring (NASA/JPL, 2021). This data measures changes in Earth's gravity field over space and time. The OBP recordings represent the integrated effect of mean oceanic and atmospheric mass (NASA/JPL, 2021), and can be used to track variations in total loading above the seafloor. When comparing the anomalous low $\delta v/v$ variation, we observe a similar low OBP anomaly in December, 2013, which occurred 53 days before the $\delta v/v$ peak (Figure 1B). Furthermore, we investigate the spatial distribution of the OBP anomaly on December 16, 2013, which suggests that the anomaly becomes stronger from the northwest to the southeast direction, perpendicular to the contour lines (Figure 1A). This distribution of the OBP anomaly generally correlates with the localization of $\delta v/v$ anomalies from different station pairs (Figure 1A). For instance, the southeastern station pairs (e.g., NM01-NM03) have larger $\delta v/v$ anomalies compared to the northwestern ones (e.g., NM02-NM05, NM02-NM04). We also observe that two station pairs (NM02-NM01 and NM04-NM01) do not exhibit consistent low $\delta v/v$ anomalies (Figure 1A). These outliers may be due to different seismic sensitivities resulting from local topography, and they do not have a significant effect on the entire area. A possible formation of the regional OBP anomaly center is discussed further in the "Discussion" section. Based on the spatiotemporal correlation between these two independent recordings, we suggest that the anomalous $\delta v/v$ variation is likely a response to the low OBP anomaly.

We further analyze the variation in OBP and investigate the original force causing the anomalous $\delta v/v$. The variation in thermohaline (temperature and salinity) plays a significant role in integrating changes in seawater density, which primarily contribute to the variation in OBP in the oceanic section (Vallis, 2017). To begin, we gather the vertical distribution of seawater temperature and salinity from the Estimating the Circulation and Climate of the Ocean (ECCO) reanalysis (Fenty & Wang, 2020b), observing that regional averaged thermohaline changes vary across the sea surface and into the depths (Figure S6). At the low OBP anomaly, we observe a slight drop in temperature and an increase in salinity, particularly from hundreds of meters to the ocean bottom depths. Based on the contours of seawater density as a function of temperature and salinity (LeBlond, 1976), reducing temperature or increasing salinity can increase seawater density at a given applied pressure. Applying this relationship to our thermohaline observation, the increasing salinity and decreasing temperature would increase seawater density, leading to a high integrated pressure anomaly at the ocean bottom. However, the thermohaline variation contradicts our observation in December 2013. Therefore we exclude thermohaline variation in the above seawater as the main force inducing this low near-seafloor $\delta v/v$ variation.

Next, our focus shifts to the changes in mass above sea level. We obtain the daily-averaged sea level pressure (SLP) variation, which reflects the atmospheric pressure adjusted for sea level, from the ECCO reanalysis (Fenty & Wang, 2020a). In Figure 3A, we can observe a consistently low SLP anomaly in December 2013, along with a corresponding long-term trend in the GRACE-based OBP variation over the two-year period. In addition, we notice that the SLP variation is approximately three times larger than the ΔOBP, indicating that the SLP variation is likely strong enough to dominate the changes in the pressure field through a downward superposition, thus controlling the $\delta v/v$ variation near the seafloor. Once we identify SLP as a potential driving force, we directly examine the correlation between SLP and $\delta v/v$ variations. Figure 3B displays these two independent time series over the two-year period. To eliminate minor perturbations and long-term trends and clarify the main phases, we apply a filter in 5 to 15-month range. In addition to the anomalous low SLP peak in December 2013, there are two additional low anomalies in January 2012 and July 2013 (blue bars in Figure 3B). Similar to Figure 1B, we observe two more consistent low $\delta v/v$ anomalies (red bars in Figure 3B), which occur with similar time lags (63 and 34 days) after the previous two SLP anomalies. Here, we use a cross-wavelet transform to analyze the time-frequency characteristics and the correlation between SLP and $\delta v/v$ variations. This transformation utilizes a wavelet function as a bandpass filter to analyze the two target datasets in the wavelet domain (Torrence & Compo, 1998). In the cross-wavelet spectrum (Figure 3C), we observe different phase lags across the timeline and frequency band, which have been converted into a yearly period. We calculate the average time lag between these two records as 45 ($\pm$10) days. If we shift the $\delta v/v$ variation by the calculated time lag and compare it with the SLP variation (Figure 3B), the consistency between these two records becomes more evident, particularly during the two overlapping phases in July and December 2013.

Discussion

We know that the speed of seismic wave in an elastic medium depends on its bulk and shear modulus, which can be influenced by the variations in effective pressure (Dvorkin et al., 1999). If the medium has high porosity, the effective pressure is equal to the difference between pore pressure (water-saturated) and applied confining pressure (Dvorkin & Nur, 1996; Saul et al., 2013). This poroelastic mechanism is used to explain changes of $\delta v/v$ in various realistic scenarios, such as hydrologic, glaciostatic, snowstatic and barometric pressure fields (Lecocq et al., 2017; Mordret et al., 2016; Toyokuni et al., 2018; Gradon et al., 2021). Therefore, in our study of the ocean bottom, we propose that the anomalous low $\delta v/v$ variation near the seafloor is likely induced by a low sea level pressure anomaly in December 2013, which reduces the ocean bottom pressure field throughout the seawater column. Here, we attempt to simulate the $\delta v/v$ variations by invoking an analytic solution for pressure-induced displacements and seismic wave speeds (Tsai, 2011). We follow the basic relation:

$$\delta v/v(t) \propto A(t) \propto \Delta P(t) \approx \Delta OBP(t - \Delta t) \quad , \tag{2}$$

where $A(t)$ represents the amplitude changes of pressure-induced displacements. Here, we assume that the pore pressure is constant near the seafloor and use the variations in applied ocean bottom pressure, $\Delta OBP(t)$, to approximate the effective pressure, $\Delta P(t)$, on the seismic field. Δt represents the time lag of $\delta v/v(t)$ with respect to the applied pressure, as observed in Figures 1B and 3. We use the peak-to-peak ΔOBP value during the anomalous period (December 2013) as the maximum effect to approximate the major phase of the $\delta v/v$ variation, as observed and measured in Figure 3C. More details about the poroelastic $\delta v/v$ simulation can be found in Text S2. All parameters used for the simulation are either from references or our investigation, and can be found in Table S2.

The simulated $\delta v/v$ from the best-fitted poroelastic model is presented in Figure 4. We observe consistent amplitudes and phases with respect to the measured $\delta v/v$. In addition to poroelasticity, previous studies consider temperature as another major factor that induces $\delta v/v$ changes through a thermoelastic mechanism (Meier et al., 2010; Tsai, 2011; Lecocq et al., 2017; Zhang et al., 2023). Therefore, we also simulate the thermoelastic $\delta v/v$ variations based on a similar mathematical framework with a substitution of temperature driving (Text S2). Comparatively, the magnitude of the thermoelastic $\delta v/v$ is much lower than that from the poroelastic simulation. This weak temperature-induced velocity change is likely due to the tiny temperature variation observed in deep seawater (Figure S6). We acknowledge that some parameter selections may involve large uncertainties, such as searching for the Murnaghan constant and diffusivity of ocean sediments (Figure S7). However, poroelasticity still provides a mathematical framework that allows us to quantify the correlation between seismic velocity and pressure variation by using all parameters within reasonable ranges. Therefore, the simulation of $\delta v/v$ further supports that the variation in ΔOBP is the dominant force inducing the observed $\delta v/v$ variation near the seafloor.

Different from the direct correlation between seismic velocities and barometric pressures in a desert environment (Gradon et al., 2021), we observed a time lag (Δt) of $\delta v/v$ with respect to the pressure field variations (Figures 1B and 3). This time lag, Δt, can be attributed to a top layer of incompetent material, which behaves in a ductile manner under stress and tends to delay the strain response to the surface field (Ben-Zion & Leary, 1986). In the ocean bottom, wind and water transport eroded grids and deposit it as sedimentary layers. This layer of ocean sediment is globally distributed and can be deformed tectonically, re-deposited or subducted (Straume et al., 2019). Therefore, this layer of ocean sediment on top of the seafloor, which has an average thickness of 288 m in the study area (Figure S8), likely plays a key role in the lag of $\delta v/v$ variations. The time lag, Δt, in poroelasticity can be quantified as (Tsai, 2011):

$$\Delta t = \frac{z_s}{\sqrt{2\omega\kappa_s}} + \frac{cot^{-1}\left(\frac{\kappa_{hy}k^2}{\omega}\right)}{2\omega} \quad , \tag{3}$$

where z_s and κ_s represent the thickness and hydraulic diffusivity of the incompetent layer, which primarily determine the value of Δt. ω and k are the angular frequency and horizontal wavenumber, respectively, and κ_{hy} is the hydraulic diffusivity of the upper crust. In our best-fitted poroelastic model, we calculated $\Delta t = 10$ days, which is shorter than the observed value of 53 days (Figure 1B). It should be noted that the observed Δt in Figure 3C is compared to the sea level instead of the ocean bottom pressure variation, and the sea level pressure variations may need time to diffuse through the seawater column and then affect the ocean bottom. One possible reason for the inconsistent Δt value is the monthly sampling of the GRACE-based OBP datasets, which may miss some short-term pressure records. This low sampling rate of the OBP datasets may also bias the pressure anomaly that we used in the $\delta v/v$ simulation. Another possible reason is that we calculated Δt by searching for some parameters (Figure S7) with respect to the filtered periodic $\delta v/v$ variation (Figure 3B). However, the realistic cycle period is not clear enough due to high-frequency variations and short data records. These discrepancies in the $\delta v/v$ simulation may introduce additional uncertainties to the estimation of Δt.

Both our observations and physical simulations support the idea that the low anomaly in $\delta v/v$ near the seafloor is likely a response to the low OBP anomaly in December 2013, which is caused by the drop in SLP in the atmosphere. The variations in the oceanic pressure field are widely associated with atmospheric activities (Gill & Niller, 1973; Wunsch & Stammer, 1997). Slingo et al. (2014) have noted that during December and January 2013/14, the Asian-Pacific jet stream, characterized by strong westerly winds, extended into the northwestern Pacific and close to Japan. This jet stream tends to generate cyclones (local/regional low-pressure centers) on its flank due to its symbiotic relationship with depressions (Slingo et al., 2014). Based on the global wind field map from the ECCO (Fenty & Wang, 2020a) on December 16, 2013, we can observe that our study area is located in the strong westerly wind belt in the northern hemisphere (Figure 5A). On a regional scale, the counterclockwise wind field likely generates a cyclone at the sea surface, with central weak winds and surrounding strong winds (Figure 5B). This low SLP anomaly could be further transported by the wind-driven friction forces (i.e., the Ekman transport) into the deep ocean bottom. A consistent regional OBP field supports this idea, showing that the pressure anomaly tends to be disaggregated and partially reduced after being transported into over 5,500 m depths (Figure 5C). A general anti-correlation between the long-term trends of SLP and wind speed (Figure S9) suggests that these low OBP anomalies easily occur in winters when the westerly winds are strong. Therefore, our ASN measurements likely include more information that reflects atmospheric activities. We acknowledge that our analysis is mainly based on off-shore ocean basins, while coastal regions may involve more complex processes that affect $\delta v/v$ variations due to interactions between seawater and land. We also observe a notable absence of long-term deep ocean bottom seismic recordings, which may be attributed to difficulties in deploying and maintaining stations. Currently, it is still challenging to attain continuous, long-term monitoring of $\delta v/v$ for ocean basins. Moreover, it is necessary to confirm the time delay in $\delta v/v$ responses to pressure changes for certain time-sensitive monitoring. Therefore, we eagerly anticipate following improvements in this ocean seismic sensing.

Conclusion

We collect two-year recordings of ambient seismic noise from five ocean bottom seismometers in the northwestern Pacific Ocean basin. Coda wave interferometry is used to measure the variation in near-seafloor relative velocity ($\delta v/v$). The time series of measured $\delta v/v$ includes a low-velocity variation, which likely corresponds to a low ocean bottom pressure anomaly in December 2013. We then successfully apply a poroelastic mechanism to explain how the variations in the pressure field induce the observed $\delta v/v$. However, we argue that the $\delta v/v$ is not always primarily influenced by the pressure field, especially in coastal or tectonically active ocean regions. Furthermore, we propose that the observed low-pressure variation may originate from the atmospheric wind field, establishing a potential connection between seismic measurements and remote atmospheric activities. Our study offers a new perspective on utilizing seismic remote sensing to monitor changes in ocean bottom basins. In the future, we anticipate that the $\delta v/v$ technique can serve as an effective tool for ocean monitoring through widespread station distribution and long-term deployment.

Data Availability Statement

Continuous ocean bottom seismic recordings are collected from the NOMan Project, operated by The University of Tokyo (Matsuno et al., 2017), and can be downloaded from `http://ohpdmc.eri.u-tokyo.ac.jp/`. Seismic interferometry and $\delta v/v$ measurements are performed using the MSNoise package (Lecocq et al., 2014). GRACE-based ocean bottom pressure and ECCO-based sea level pressure, sea surface wind speed, seawater temperature and salinity are released by the Physical Oceanography Distributed Active Archive Center (PODAAC) (NASA/JPL, 2021; Fenty & Wang, 2020a, 2020b), which can be downloaded from `https://podaac.jpl.nasa.gov/cloud-datasets`. All figures are plotted using the Generic Mapping Tools (GMT) 6.2.0 and Matplotlib 3.3.0 (Wessel et al., 2019; Hunter, 2007).

Acknowledgments

This research is supported by U.S. National Science Foundation Grant Number EAR2042098. We would like to express our gratitude to Dr. Dou Li for her valuable insights and productive discussions on the variations of the oceanic pressure field.

References

Ben-Zion, Y., & Leary, P. (1986, 10). Thermoelastic strain in a half-space covered by unconsolidated material. *Bulletin of the Seismological Society of America*, *76*(5), 1447-1460. doi: 10.1785/BSSA0760051447

Brenguier, F., Shapiro, N., Campillo, M., Ferrazzini, v., Duputel, Z., Coutant, O., & Nercessian, A. (2008, 01). Toward forecasting volcanic eruption using seismic noise. *Nature geoscience*, *1*. doi: 10.1038/ngeo104

Bucker, H. P. (1976, 02). Use of calculated sound fields and matched-field detection to locate sound sources in shallow water. *The Journal of the Acoustical Society of America*, *59*(2), 368-373. doi: 10.1121/1.380872

Campillo, M., & Roux, P. (2015, 12). Crust and lithospheric structure - seismic imaging and monitoring with ambient noise correlations. In (p. 391-417). doi: 10.1016/B978-0-444-53802-4.00024-5

Clarke, D., Zaccarelli, L., Shapiro, N. M., & Brenguier, F. (2011, 08). Assessment of resolution and accuracy of the Moving Window Cross Spectral technique for monitoring crustal temporal variations using ambient seismic noise. *Geophysical Journal International*, *186*(2), 867-882. doi: 10.1111/j.1365-246X.2011.05074.x

Dvorkin, J., Mavko, G., & Nur, A. (1999). Overpressure detection from compressional- and shear-wave data. *Geophysical Research Letters*, *26*(22), 3417-3420. doi: https://doi.org/10.1029/1999GL008382

Dvorkin, J., & Nur, A. (1996, 10). Elasticity of high-porosity sandstones; theory for two North Sea data sets. *Geophysics*, *61*(5), 1363-1370. doi: 10.1190/1.1444059

Fenty, I., & Wang, O. (2020a). *Ecco atmosphere surface temperature, humidity, wind, and pressure - daily mean 0.5 degree (version 4 release 4).* NASA Physical Oceanography Distributed Active Archive Center. Retrieved from `https://podaac.jpl.nasa.gov/dataset/ECCO_L4_ATM_STATE_05DEG_DAILY_V4R4` doi: 10.5067/ECG5D-ATM44

Fenty, I., & Wang, O. (2020b). *Ecco ocean temperature and salinity - daily mean 0.5 degree (version 4 release 4).* NASA Physical Oceanography Distributed Active Archive Center. Retrieved from `https://podaac.jpl.nasa.gov/dataset/ECCO_L4_TEMP_SALINITY_05DEG_DAILY_V4R4` doi: 10.5067/ECG5D-OTS44

Gill, A., & Niller, P. (1973). The theory of the seasonal variability in the ocean. *Deep Sea Research and Oceanographic Abstracts*, *20*(2), 141-177. Retrieved from `https://www.sciencedirect.com/science/article/pii/0011747173900491` doi: https://doi.org/10.1016/0011-7471(73)90049-1

Gradon, C., Brenguier, F., Stammeijer, J., Mordret, A., Hindriks, K., Campman, X., ... Chmiel, M. (2021, 07). Seismic Velocity Response to Atmospheric Pressure Using Time-Lapse Passive Seismic Interferometry. *Bulletin of the Seismological Society of America*, *111*(6), 3451-3458. doi: 10.1785/0120210069

Gutenberg, B. (1958). Microseisms. In H. Landsberg & J. Mieghem (Eds.), (Vol. 5, p. 53-92). Elsevier. Retrieved from `https://www.sciencedirect.com/science/article/pii/S0065268708600758` doi: https://doi.org/10.1016/S0065-2687(08)60075-8

Hadziioannou, C., Larose, E., Coutant, O., Roux, P., & Campillo, M. (2009, 06). Stability of monitoring weak changes in multiply scattering media with ambient noise correlation: Laboratory experiments. *The Journal of the Acoustical Society of America*, *125*(6), 3688-3695. doi: 10.1121/1.3125345

Hunter, J. D. (2007). Matplotlib: A 2d graphics environment. *Computing in Science & Engineering*, *9*(3), 90–95. doi: 10.1109/MCSE.2007.55

Igel, J. K. H., Bowden, D. C., & Fichtner, A. (2023). Sans: Publicly available daily multi-scale seismic ambient noise source maps. *Journal of Geophysical Research: Solid Earth*, *128*(1), e2022JB025114. doi: https://doi.org/10.1029/2022JB025114

LeBlond, P. (1976). Temperature–salinity analysis of world ocean waters. *Journal of the Fisheries Board of Canada*, *33*(6), 1471–1471.

Lecocq, T., Caudron, C., & Brenguier, F. (2014). MSNoise, a python package for monitoring seismic velocity changes using ambient seismic noise. *Seismological Research Letters*, *85*(3), 715-726. doi: 10.1785/0220130073

Lecocq, T., Longuevergne, L., Pedersen, H., Brenguier, F., & Stammler, K. (2017, 10). Monitoring ground water storage at mesoscale using seismic noise: 30 years of continuous observation and thermo-elastic and hydrological modeling. *Scientific Reports*, *7*. doi: 10.1038/s41598-017-14468-9

Lin, F.-C., Ritzwoller, M. H., Townend, J., Bannister, S., & Savage, M. K. (2007, 08). Ambient noise Rayleigh wave tomography of New Zealand. *Geophysical Journal International*, *170*(2), 649-666. doi: 10.1111/j.1365-246X.2007.03414.x

Luo, B., Zhang, S., & Zhu, H. (2023). Monitoring seasonal fluctuation and long-term trends for the greenland ice sheet using seismic noise auto-correlations. *Geophysical Research Letters*, *50*(7), e2022GL102146. doi: https://doi.org/10.1029/2022GL102146

Mao, S., Lecointre, A., van der Hilst, R., & Campillo, M. (2022). Space-time monitoring of groundwater fluctuations with passive seismic interferometry. *Nature Communications*, *13*, 4643. doi: 10.1038/s41467-022-32194-3

Matsuno, T., Suetsugu, D., Baba, K., Tada, N., Shimizu, H., Shiobara, H., ... Utada, H. (2017). Mantle transition zone beneath a normal seafloor in the northwestern pacific: Electrical conductivity, seismic thickness, and water content. *Earth and Planetary Science Letters*, *462*, 189-198. Retrieved from `https://www.sciencedirect.com/science/article/pii/S0012821X16307580` doi: https://doi.org/10.1016/j.epsl.2016.12.045

Meier, U., Shapiro, N. M., & Brenguier, F. (2010, 05). Detecting seasonal variations in seismic velocities within Los Angeles basin from correlations of ambient seismic noise. *Geophysical Journal International*, *181*(2), 985-996. doi: 10.1111/j.1365-246X.2010.04550.x

Mordret, A., Mikesell, T. D., Harig, C., Lipovsky, B. P., & Prieto, G. A. (2016). Monitoring southwest Greenland's ice sheet melt with ambient seismic noise. *Science Advances*, *2*(5), e1501538. doi: 10.1126/sciadv.1501538

NASA/JPL. (2021). *Jpl tellus grace level-3 monthly ocean bottom pressure anomaly release 6.0 version 04 in netcdf/ascii/geotiff formats.* NASA Physical Oceanography Distributed Active Archive Center. Retrieved from `https://podaac.jpl.nasa.gov/dataset/TELLUS_GRAC_L3_JPL_RL06_OCN_v04` doi: 10.5067/TEOCN-3AJ64

Nishida, K., Kawakatsu, H., & Obara, K. (2008). Three-dimensional crustal s wave velocity structure in japan using microseismic data recorded by hi-net tiltmeters. *Journal of Geophysical Research: Solid Earth*, *113*(B10). doi: https://doi.org/10.1029/2007JB005395

Ratdomopurbo, A., & Poupinet, G. (1995). Monitoring a temporal change of seismic velocity in a volcano: Application to the 1992 eruption of mt. merapi (indonesia). *Geophysical Research Letters*, *22*(7), 775-778. doi: https://doi.org/10.1029/95GL00302

Sabra, K., Roux, P., & Kuperman, W. (2005, DEC). Emergence rate of the time-domain green's function from the ambient noise cross-correlation function. *JOURNAL OF THE ACOUSTICAL SOCIETY OF AMERICA*, *118*(6), 3524-3531. doi: 10.1121/1.2109059

Saul, M., Lumley, D., & Shragge, J. (2013). Modeling the pressure sensitivity of uncemented sediments using a modified grain contact theory: Incorporating grain relaxation and porosity effects. *GEOPHYSICS*, *78*(5), D327-D338. doi: 10.1190/geo2012-0459.1

Scholte, J. G. (1947, 05). The Range of Existence of Rayleigh and Stoneley Waves.

Geophysical Supplements to the Monthly Notices of the Royal Astronomical Society, *5*(5), 120-126. doi: 10.1111/j.1365-246X.1947.tb00347.x

Sens-Schönfelder, C., & Wegler, U. (2006a). Passive image interferometry and seasonal variations of seismic velocities at Merapi Volcano, Indonesia. *Geophysical Research Letters*, *33*(21). doi: https://doi.org/10.1029/2006GL027797

Sens-Schönfelder, C., & Wegler, U. (2006b). Passive image interferometry and seasonal variations of seismic velocities at merapi volcano, indonesia. *Geophysical Research Letters*, *33*(21). doi: https://doi.org/10.1029/2006GL027797

Shapiro, N. M., Campillo, M., Stehly, L., & Ritzwoller, M. H. (2005). High-resolution surface-wave tomography from ambient seismic noise. *Science*, *307*(5715), 1615-1618. doi: 10.1126/science.1108339

Slingo, J., Belcher, S., Scaife, A., McCarthy, M., Saulter, A., McBeath, K., ... Parry, S. (2014, February). *The recent storms and floods in the uk* (Tech. Rep.). Exeter. Retrieved from `http://nora.nerc.ac.uk/id/eprint/505192/` (Freely available online - Official URL link provides full text.)

Straume, E. O., Gaina, C., Medvedev, S., Hochmuth, K., Gohl, K., Whittaker, J. M., ... Hopper, J. R. (2019). Globsed: Updated total sediment thickness in the world's oceans. *Geochemistry, Geophysics, Geosystems*, *20*(4), 1756-1772. doi: https://doi.org/10.1029/2018GC008115

Torrence, C., & Compo, G. P. (1998). A practical guide to wavelet analysis. *Bulletin of the American Meteorological Society*, *79*(1), 61 - 78. doi: https://doi.org/10.1175/1520-0477(1998)079⟨0061:APGTWA⟩2.0.CO;2

Toyokuni, G., Takenaka, H., Takagi, R., Kanao, M., Tsuboi, S., Tono, Y., ... Zhao, D. (2018). Changes in greenland ice bed conditions inferred from seismology. *Physics of the Earth and Planetary Interiors*, *277*, 81-98. doi: https://doi.org/10.1016/j.pepi.2017.10.010

Tsai, V. C. (2011). A model for seasonal changes in gps positions and seismic wave speeds due to thermoelastic and hydrologic variations. *Journal of Geophysical Research: Solid Earth*, *116*(B4). doi: https://doi.org/10.1029/2010JB008156

Vallis, G. K. (2017). *Atmospheric and oceanic fluid dynamics*. Cambridge University Press.

Wegler, U., & Sens-Schönfelder, C. (2007, 03). Fault zone monitoring with passive image interferometry. *Geophysical Journal International*, *168*(3), 1029-1033. doi: 10.1111/j.1365-246X.2006.03284.x

Wessel, P., Luis, J. F., Uieda, L., Scharroo, R., Wobbe, F., Smith, W. H. F., & Tian, D. (2019). The generic mapping tools version 6. *Geochemistry, Geophysics, Geosystems*, *20*(11), 5556-5564. doi: https://doi.org/10.1029/2019GC008515

Wu, W., Zhan, Z., Peng, S., Ni, S., & Callies, J. (2020). Seismic ocean thermometry. *Science*, *369*(6510), 1510-1515. doi: 10.1126/science.abb9519

Wunsch, C., & Stammer, D. (1997). Atmospheric loading and the oceanic "inverted barometer" effect. *Reviews of Geophysics*, *35*(1), 79-107. doi: https://doi.org/10.1029/96RG03037

Yang, Y., Ritzwoller, M. H., Levshin, A. L., & Shapiro, N. M. (2007, 01). Ambient noise Rayleigh wave tomography across Europe. *Geophysical Journal International*, *168*(1), 259-274. doi: 10.1111/j.1365-246X.2006.03203.x

Yao, H., van Der Hilst, R. D., & de Hoop, M. V. (2006, 08). Surface-wave array tomography in SE Tibet from ambient seismic noise and two-station analysis — I. Phase velocity maps. *Geophysical Journal International*, *166*(2), 732-744. doi: 10.1111/j.1365-246X.2006.03028.x

Zhan, Z., Tsai, V. C., & Clayton, R. W. (2013, 05). Spurious velocity changes caused by temporal variations in ambient noise frequency content. *Geophysical Journal International*, *194*(3), 1574-1581. doi: 10.1093/gji/ggt170

Zhang, S., Luo, B., Ben-Zion, Y., Lumley, D. E., & Zhu, H. (2023). Monitoring terrestrial water storage, drought and seasonal changes in central oklahoma with ambient seismic noise. *Geophysical Research Letters*, *50*(17), e2023GL103419.

doi: https://doi.org/10.1029/2023GL103419

A

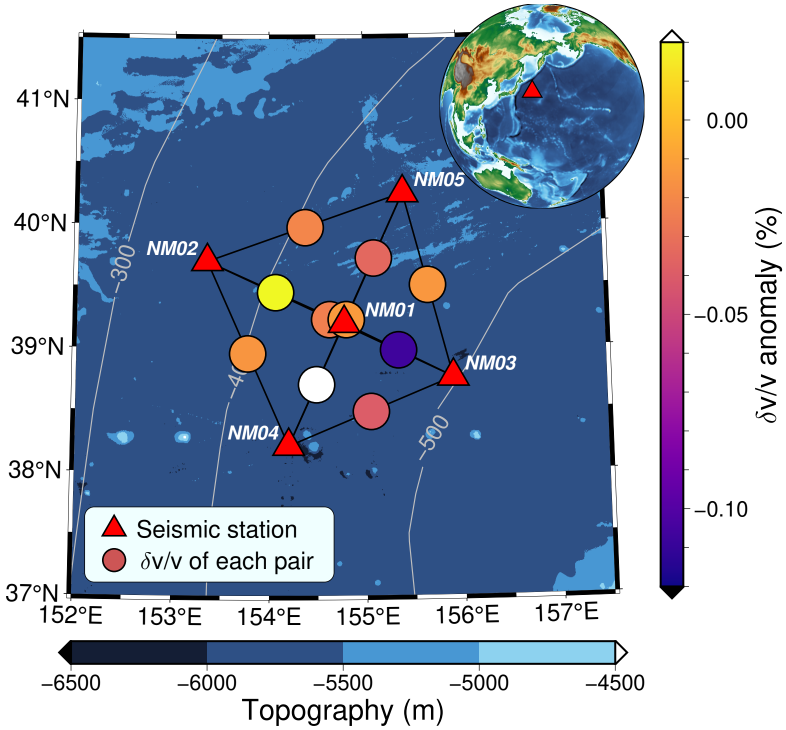

B

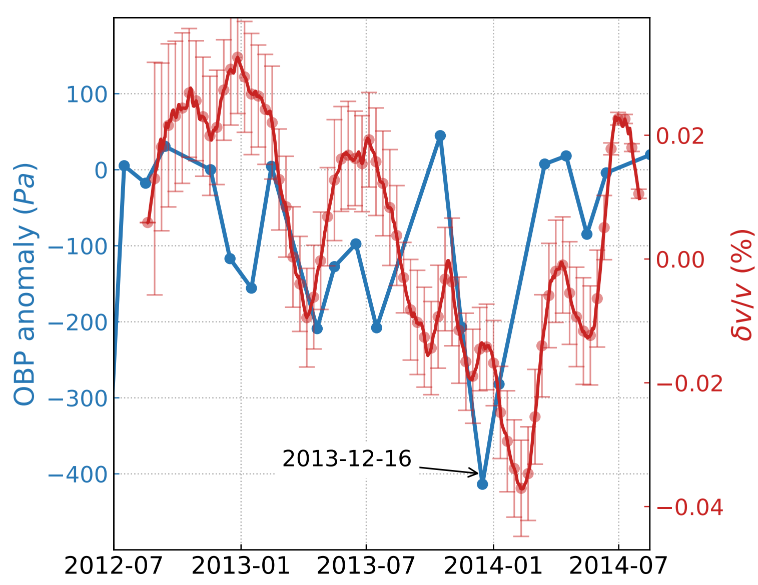

Figure 1: Spatiotemporal distribution of anomalous seismic velocity ($\delta v/v$) and ocean bottom pressure (OBP). Panel (A) displays the measured $\delta v/v$ anomaly for each station pair. The circle at the mid-point of each pair is color-coded based on the $\delta v/v$ anomaly in February 2014. Gray contour lines represent the OBP anomalies (in Pascal) on December 16, 2013, with respect to November 2012. Panel (B) illustrates the temporal evolution of the variations in $\delta v/v$ and the OBP anomaly within the study area. The OBP records are sampled on a monthly basis, and the $\delta v/v$ time series is smoothed using a 30-day running mean.

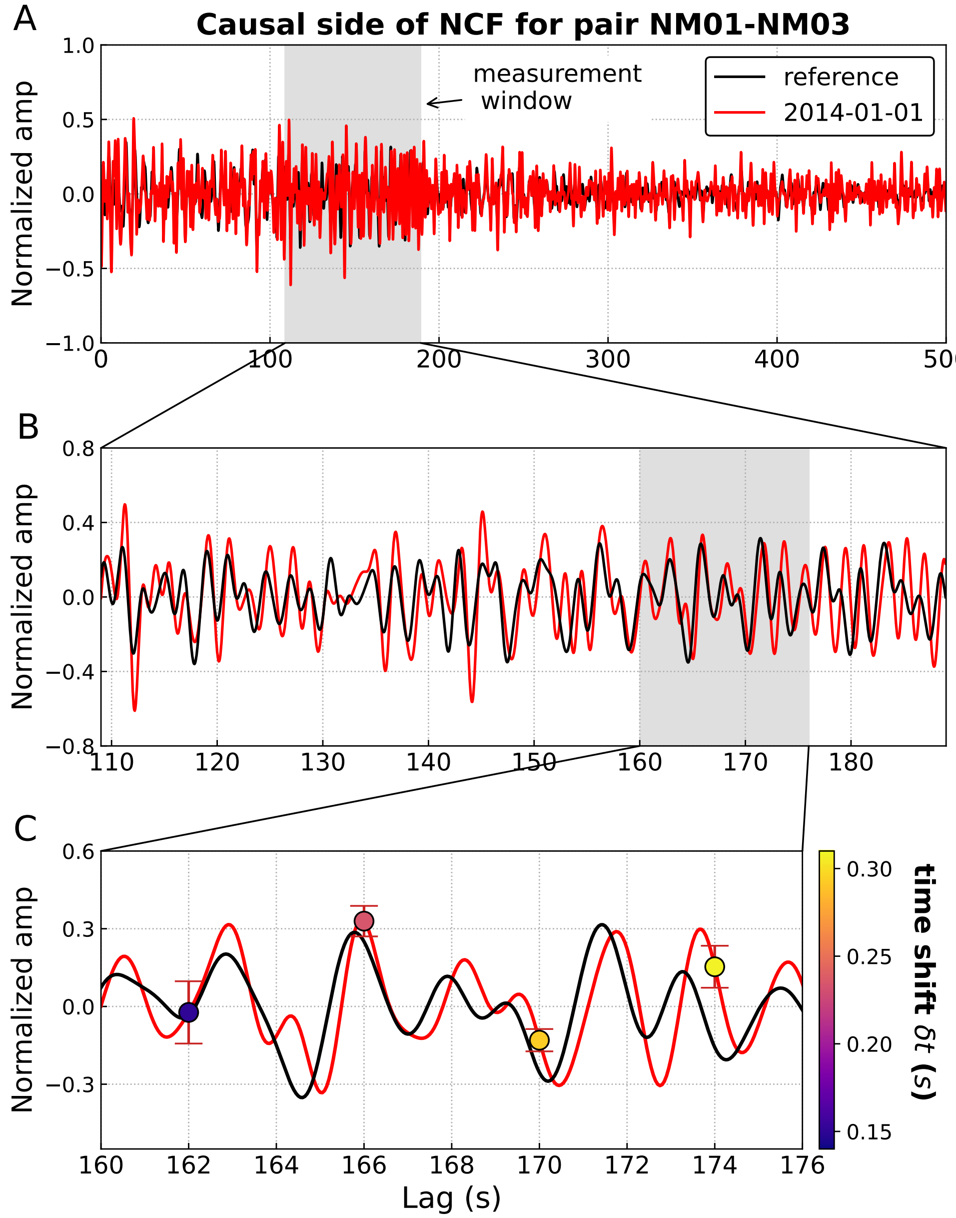

Figure 2: An example illustrating the shift in traveltime between a daily measurement taken on 2014-01-01 and the reference NCFs for the station pair NM01-NM03. Panel (A) displays the causal sides of these two NCFs. The gray shade represents the measurement window defined by a phase velocity of 1.0 km/s and a window length of 80 s. Panel (B) provides close-up views for the measurement window in (A). Panel (C) provides close-up views of a typical window in (B). Time shifts (δt), represented by colored circles, are shown at four steps in the daily NCF. These δt values are measured in the Fourier domain by using MWCS analysis. The error bars indicate double measurement misfits.

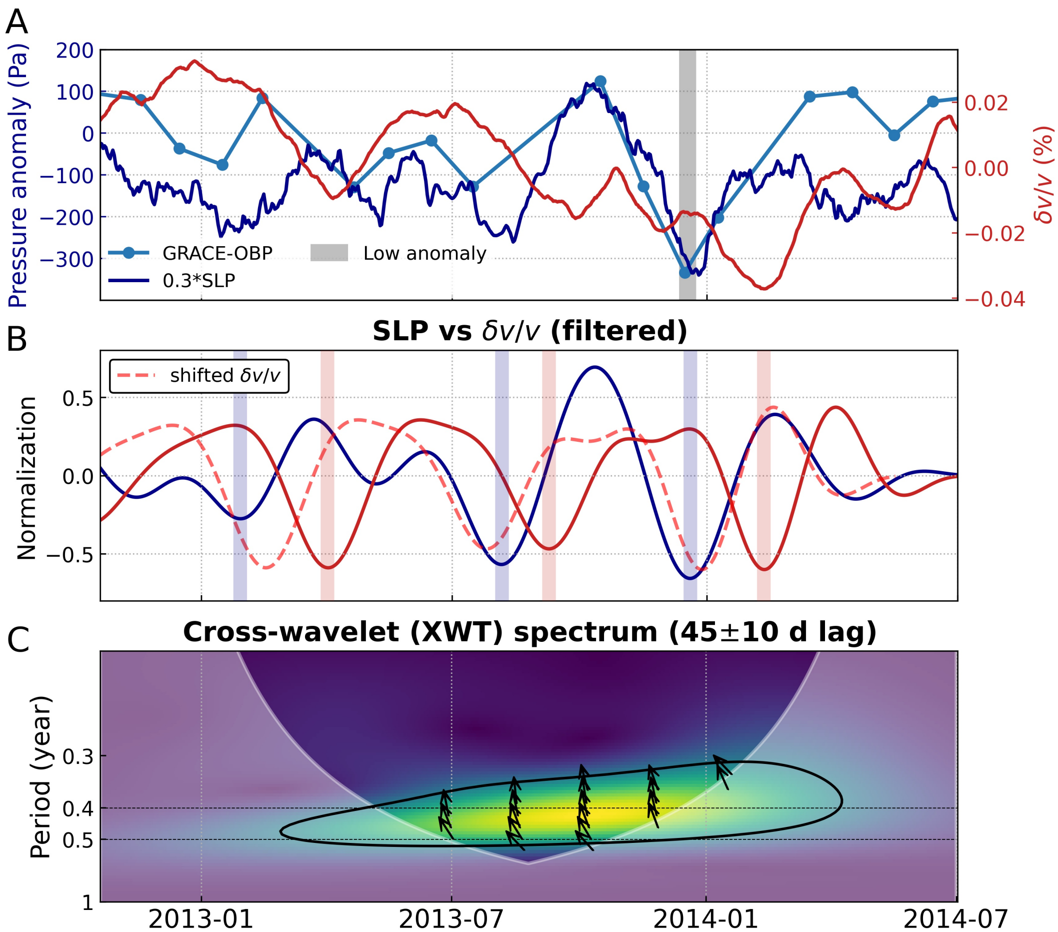

Figure 3: Correlation between the variations in relative seismic velocity and pressure field. Panel (A) compares the time series of ocean bottom pressure (OBP, in dotted cyan), sea level pressure (SLP, in dark blue) and $\delta v/v$ (in red). The gray bar denotes the low-pressure anomaly in December 2013. Panel (B) compares the major phases of SLP (in dark blue) and $\delta v/v$ (in red). Both datasets are normalized and filtered in 5 to 15 months. We use blue and red bars to denote their low anomalies. The dashed red curve is the shifted $\delta v/v$ with the measured lag in Panel (C). Panel (C) presents the cross-wavelet spectrum between SLP and $\delta v/v$. The white shade represents the influential edge effects, and the black contour represents a 98% confidence level. Arrows denote local phase angles with periods in vertical axis. The measured $\delta v/v$ time lag (45 ± 10 days) is averaged over selected phases in the spectrum.

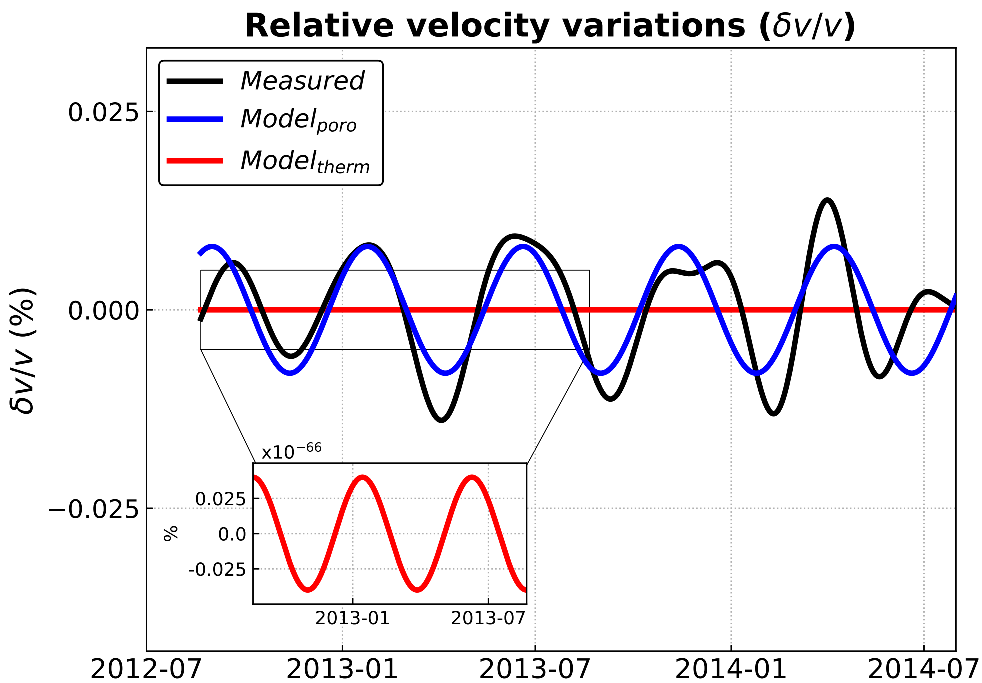

Figure 4: Simulations of the near-seafloor relative seismic velocity variation. The black curve represents the filtered measured $\delta v/v$, which is the same as the one shown in Figure 3B. We present the simulated $\delta v/v$ from the best fit poroelastic (in blue) and thermoelastic (in red) models. The inset panel provides a close-up view of the simulated thermoelastic $\delta v/v$ in the boxed segment. It is important to note the relatively small amplitudes in comparison to the other two from the poroelastic simulation and measurement.

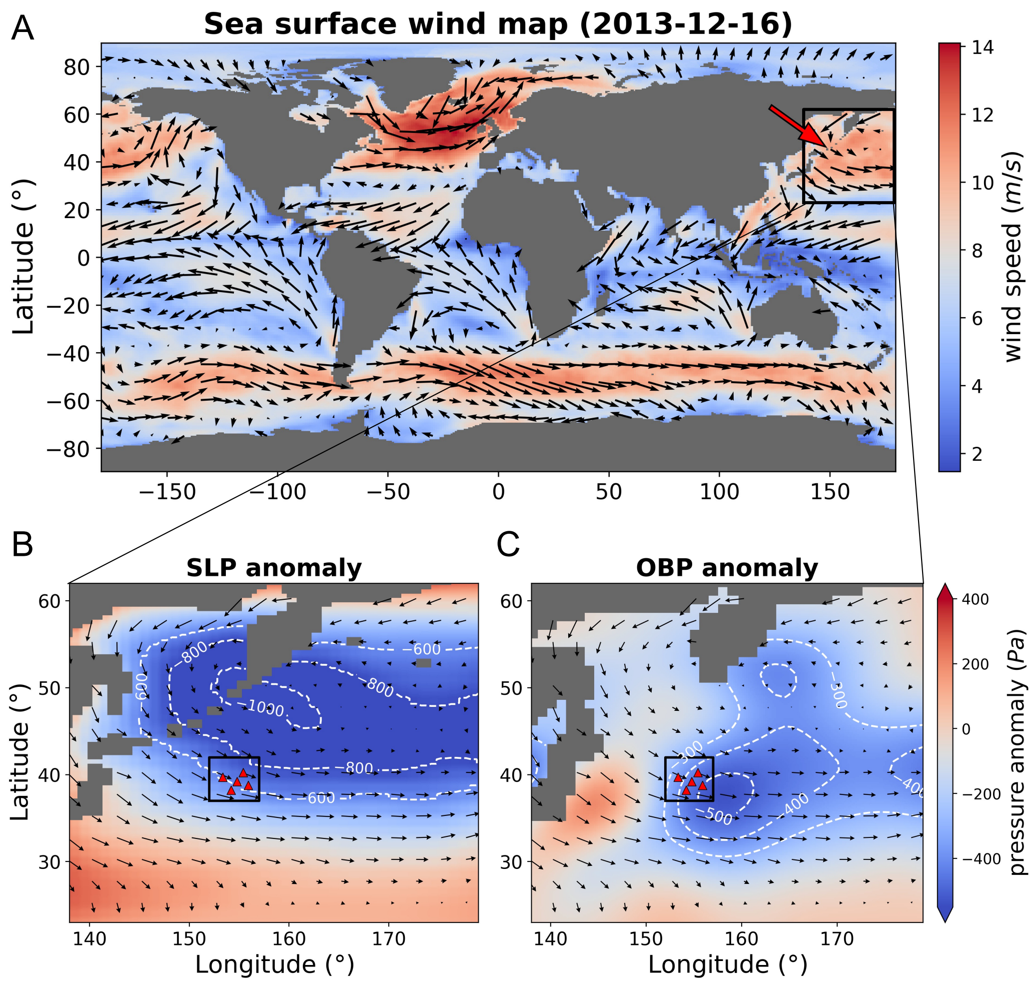

Figure 5: Correlation between the variations in the regional wind and pressure fields. Panel A displays the global distribution of the sea surface wind speed on December 16, 2013. The black arrows correspond to the wind vectors that are associated with the background colors. The bold red arrow and black box indicates our study area. The gray area represents land. Panels B and C illustrate the regional variations in sea level (SLP) and ocean bottom (OBP) fields, respectively, which are associated with the wind vectors shown in the black box in Panel A. Please note the symbiosis between low pressure centers and the likely cyclone.